Icarus **154**, 501–515 (2001)
doi:10.1006/icar.2001.6643, available online at http://www.idealibrary.com on IDEAL®

Images of Titan at 1.3 and 1.6 μm with Adaptive Optics at the CFHT

Athena Coustenis and Eric Gendron

Department for Space Research, Observatoire de Paris-Meudon, 92195 Meudon Cedex, France
E-mail: athena.coustenis@obspm.fr

Olivier Lai

Canada–France–Hawaii Telescope, Hawaii 96743

Jean-Pierre Véran

Herzberg Institute of Astrophysics, National Research Council, Canada

Julien Woillez, Michel Combes, and Loic Vapillon

DESPA, Observatoire de Paris-Meudon, 92195 Meudon Cedex, France

Thierry Fusco and Laurent Mugnier

ONERA/DOTA, 92322 Châtillon, France

and

Pascal Rannou

Service d'Aéronomie, Univ. Versailles-St Quentin, France

Received October 26, 2000; revised April 11, 2001

Titan was observed with the Adaptive Optics Bonette at the Canada–France–Hawaii Telescope during October 27th 1998 (UTC), when the satellite was at greatest eastern elongation (GEE) with respect to Saturn and its leading hemisphere was seen from the Earth. The seeing was excellent during these observations (with peaks at 0.3″ in the visible), and this allowed us to successfully image Titan for the first time in the J band, where the adaptive optics correction is highly dependent on the atmospheric conditions. Images were obtained in the center of the so-called "methane windows," where the absorption is weak (at 1.29 –J1– and 1.6 μm –H1–) and also in the wings of the CH_4 bands (at 1.18 μm –J2– and 1.64 μm –H2–) with narrowband filters. The latter wavelengths yield information on Titan's stratosphere and allow us, by subtracting its contribution from the J1 and H1 images, to infer furthermore direct information on the surface properties. The resolution on the J and H diffraction-limited images is about 0.08–0.1″, translating into about 10 independent resolution elements or 20 pixels on the Titan disk. We have obtained reconstructed PSFs of very high signal-to-noise ratio, with associated Strehl ratios of about 35% in J and 50% in H. Hence, new and more efficient deconvolution methods (such as MISTRAL) were applied to the images, reducing ringing defects and restoring the initial photometry while enhancing the contrast on the observed features. Thus, the main features of the Titan atmosphere (bright south pole) and surface (large bright equatorial region and darker areas)—as previously observed with ADONIS/ESO, as well as with the HST and the Keck telescopes—are apparent, but with a much higher level of detail and contrast (about 30%) at these wavelengths. In addition, on the J1 and J2 images, along with the north–south asymmetry (which is probably due to seasonal effects), another bright feature is reported for the first time seen on Titan's morning limb (anti-Saturn during GEE). This feature may be diagnostic of diurnal effects (such as morning fog) at altitudes of 70–90 km (due to the cycle of the condensable species), but requires further investigation before its origin can be firmly identified. On the surface images (corrected for limb effects and atmospheric contribution), the large equatorial feature is found to be bright also at 1.3 μm (thus further constraining models of the surface composition). The high quality of the data allows us to resolve this area into three or more individual peaks, possibly towering over a mountainous plateau covered with ice (a plausible candidate being ethane ice). In any event, our images show this part of Titan's leading hemisphere to be more complex than previously suggested by models of Titan's surface. From our albedo maps, it appears that the darker areas have reflectances that are about three times lower than the bright equatorial region.

Key Words: **Titan; satellites, atmospheres; surfaces, satellite; infrared observations.**

0019-1035/01 $35.00

1. INTRODUCTION

Observations of Titan in the near infrared have been continuously exercised from the ground for almost a decade now, bringing new, exciting information on the atmosphere and surface of the satellite. In combination with images from the HST, the Earth-based Titan data place constraints on the possible nature of a surface that has avoided direct detection in the visible even by space missions due to a very efficient backscattering by stratospheric aerosols. In contrast, in the near-infrared, the scattering optical depth of the Titan haze is smaller than in the visible or the ultraviolet (by factors of 3–10) (Rages *et al*. 1983; Tomasko 1984; Griffith *et al*. 1991). The submicrometer particles scatter light more efficiently at shorter than at longer wavelengths. Furthermore, the atmospheric regions reached by the incident light depend essentially on the strength of the methane absorption bands. This absorption varies considerably with wavelength, thus giving access to different altitude levels that can be probed in the atmosphere. There exist in the near-IR several spectral windows where the absorption of methane is weak enough and the atmosphere sufficiently transparent to allow sounding of the surface.

Due to its small angular diameter (0.8 arcsec), comparable to the mean value of the seeing at good observing sites, Titan can be spatially resolved from the Earth's orbit only thanks to the HST (Smith *et al*. 1996; Meier *et al*. 2000) and from the ground by means of adaptive optics in the near-infrared (as was demonstrated when the first spatially resolved images of the satellite were obtained using the ADONIS prototype (COME-ON) by Saint-Pé *et al*. (1993)), or by speckle imaging (Gibbard *et al*. 1999). In the case of Titan, the adaptive optics and speckle images efficiently compete with observations made by the HST (e.g., Combes *et al*. 1997a).

The ADONIS adaptive optics system, located at the ESO telescope in Chile, has previously been used for Titan observations in the H and K bands since 1994 (Combes *et al*. 1997a). Titan's atmosphere is less affected by scattering at 2 μm than at shorter wavelengths. As a consequence, we first observed Titan with ADONIS in the 2-μm band despite a lower incoming solar flux. Since then, taking the Earth's atmospheric transmission into account, ADONIS has covered various orbital phases on Titan and different wavelength regions (around 1.6 and 2.0 μm), with narrowband filters situated in the methane atmospheric windows (H1 and K1), that is, outside the strong methane absorption bands. We have also acquired data in the wings of these bands (H2 and K2) in order to retrieve information on the Titan atmospheric properties at these wavelengths and to be able to constrain the atmospheric contribution on our images. Subtracting the "atmospheric" images from the "window" images gives us access to Titan's surface.

Both the leading and the trailing hemispheres of Titan were observed with ADONIS. The 2-μm surface images (Combes *et al*. 1997a) showed a broad bright equatorial region on Titan's leading hemisphere centered near 114° LCM, extending over roughly 30° in latitude and 60° in longitude in accordance with HST results (Smith *et al*. 1996) and spectroscopic measurements indicative of a much brighter leading rather than trailing side (Lemmon *et al*. 1993; Griffith 1993; Coustenis *et al*. 1995). This region was resolved into several (3 or perhaps more) distinct areas. The surface of Titan's trailing hemisphere at 2.0 μm as seen on the ADONIS images was not completely dark, but showed bright zones near the poles, with the larger and brighter (by factors of about 2) area near the north pole (Combes *et al*. 1997a).

ADONIS was also used in 1995, 1996, and 1997 to observe Titan in the H and K bands, with the H1, H2, K1, and K2 narrowband filters (at 1.6, 1.65, 2.0, and 2.2 μm) and with circular variable filters (CVFs) during several consecutive nights (Combes *et al*. 1997b). Titan was not observed with ADONIS in the windows near 1 μm, due to the system's limited efficiency at short wavelengths.

Observing Titan at short wavelengths with adaptive optics, thus complementing the ADONIS observations, became possible with the advent of PU'EO at the CFHT.

2. THE PU'EO ADAPTIVE OPTICS IMAGES

2.1. Adaptive Optics Systems

Adaptive optics (AO) was developed in order to compensate in real time for the effects of the atmospheric turbulence on the imaging quality and to restore nearly diffraction-limited images (Gendron and Léna 1994, 1995). The improved resulting images can be furthermore optimized by means of *a posteriori* deconvolution by the point spread function (PSF) at the time of the observations.

In imaging Titan, we used two different AO systems, both developed with the contribution of the Space Research Department of Paris Observatory (DESPA). In the first one, ADONIS, implemented on the 3.6-m ESO telescope in Chile (Rigaut *et al*. 1991; Saint-Pé *et al*. 1993), the departures of the actual wavefront from its ideal figure are continuously measured in a set of subapertures into the telescope pupil by a Shark–Hartmann wavefront sensor using a CCD detector array. They are compensated at high time rate by opposite phase variations through deformations of a very thin mirror, induced by linear motors in a set of discrete points conjugated with the subapertures. The PSF is obtained from stellar images recorded just before and after the acquisition of Titan (some seconds of exposure time). ADONIS is well adapted for correcting significant phase defects for a large number of spatial modes of the wavefront distorsions. It is then well adapted for observations at wavelengths of 1.6 or 2 μm and longer, on observing sites of moderate seeing quality.

The second one, PU'EO, implemented on the 3.6-m CFH telescope at Mauna Kea (Lai *et al*. 1997; Rigaut *et al*. 1998), is based on a different concept proposed first by Roddier *et al*. (1988). The defects of the wavefront are determined by the sensing of the local curvatures of the wavefront using Avalanche Photo

Diodes (ADP) as detectors. Their compensations are obtained by local curvatures of a deformable mirror. The PSFs are derived directly from the data accumulated by the wavefront analyzer during the Titan exposures (Véran *et al*. 1997). PU'EO is optimized for limited phase corrections and for low spatial orders of the wavefront distortions, but the use of the ADPs instead of the CCD allows for faster corrections. PU'EO takes full advantage of the usually excellent seeing conditions on Mauna Kea. It is then more efficient than ADONIS at shorter wavelengths, and in particular, in the case of Titan, in the near-1-μm methane windows.

In both cases, Titan is sufficiently bright and its angular diameter as seen from the Earth (0.854 arcsec on Oct. 26th) is sufficiently small to be used itself as the reference source for the wavefront analyzer.

For a detailed description of the PU'EO adaptive optics system and the associated camera KIR, visit http://www.cfht.hawaii.edu/instruments.

2.2. *PU'EO Observations of Titan*

We observed Titan with PU'EO at the CFHT on October 26th, 1998 Hawaiian local time (October 27, 7–13 h UTC), when Titan was at greatest eastern elongation (GEE) with respect to Saturn and the leading hemisphere was visible. Titan's diameter in the sky was 0.856 arcsec. The phase angle of our 1998 PUEO observations is -0.502°, if the Sun is considered to be the origin of the phase angle (that is, in a Sun–Titan–Earth configuration). This is indeed a small phase, but not zero, and from the work of Lockwood *et al*. (1986) on the albedo dependence on phase angle we might expect that there could be a visible effect in disk-resolved images. The subsolar point coordinates were latitude $= -15.5^\circ$ and longitude $= 92^\circ$. The subsolar point being located to the right (to the east-map) of the sub-Earth point, the phase effect would result in the eastern hemisphere (sub-Saturn at GEE) exhibiting an east-map (or evening) limb brightening.

As with ADONIS, the observing procedure consists of a set of elementary Titan images with very short exposure times (typically 1 s) recorded alternatively on two different quadrants (C1 and C3) of the bidimensional detector array (KIR) thanks to an internal scanning (on–off) mirror. The pixel size of the KIR camera is 0.035 arcsec.

During our observing night, we benefited from exceptionnally good seeing conditions, with peaks at 0.25 arcsec in the visible. The data sets from our observations of Titan and of the standard star used in photometry (see Section 3.2) are described in detail in Table I. In this study we have mainly used the higher-quality images taken between 7:00 and 10:00 h UTC on Oct. 27th, when the seeing was better than 0.5.

The atmospheric conditions allowed us to obtain diffraction-limited images in the 1.28- and 1.6-μm windows and in the methane bands. To our knowledge, the J band at this wavelength was observed for the first time. Our narrow-band filters (Fig. 1) are centered at 1.293 μm (J1), 1.59 μm (H1), 1.18 μm (J2), and 1.636 μm (H2). The full-width at half-maximum (FWHM) on these filters is about 0.15 μm for J1 and H1 and 0.10 μm for J2 and H2 (Table II). As can be seen in Fig. 1, the separation of the H1 and H2 filters is not as efficient as between J1 and J2. Hence, the H2 filter includes some contribution from the surface component of Titan.

TABLE I
Titan and Standard Star Observations on October 27th, 1998 UTC

Time (UTC)	Object	Filter	Seeing in arcsec
07:01	HD152740	H1	0.29
07:06	HD152740	H2	0.38
07:14	Titan	H2	0.44
07:34	Titan	H1	0.30
08:04	HD152740	J1	0.32
08:06	HD152740	J2	0.36
08:17	Titan	J2	0.25
08:30	Titan	J1	0.31
08:41	HD152740	J1	0.33
08:53	HD152740	J2	0.29
09:00	HD152740	H1	0.50
09:13	HD152740	H2	0.41
09:21	Titan	H2	0.54
09:39	Titan	H1	0.50
10:08	FS4	H1	0.50
10:18	FS4	H2	0.85
10:32	FS4	J1	0.91
11:37	FS4	J2	1.01
11:59	Titan	J2	0.98
12:12	Titan	J1	1.02
12:47	FS4	J2	1.01

2.3. *The Point Spread Functions*

The PSFs were obtained using the automatic AO PSF reconstruction method described in Véran *et al*. (1997) and implemented at CFHT. Unlike the traditional empirical method that relies on acquiring a guide star just after or before the science exposure, the CFHT automatic method derives the PSF directly from data accumulated by the AO system during the science exposure. Not only does this method not waste any observing time, it is also not affected by the short term seeing fluctuations,

TABLE II
Characteristics of the Filters and Other Parameters

Filter name	Wavelength center $\pm 1/2$ FWHM (μm)	Region probed	Averaged geometric albedo
J1	1.293 ± 0.075	Atmosphere and surface	0.24 ± 0.025
J2	1.180 ± 0.05	Atmosphere	0.12 ± 0.01
H1	1.590 ± 0.071	Atmosphere and surface	0.18 ± 0.02
H2	1.636 ± 0.05	Atmosphere mainly (and surface)	0.09 ± 0.01

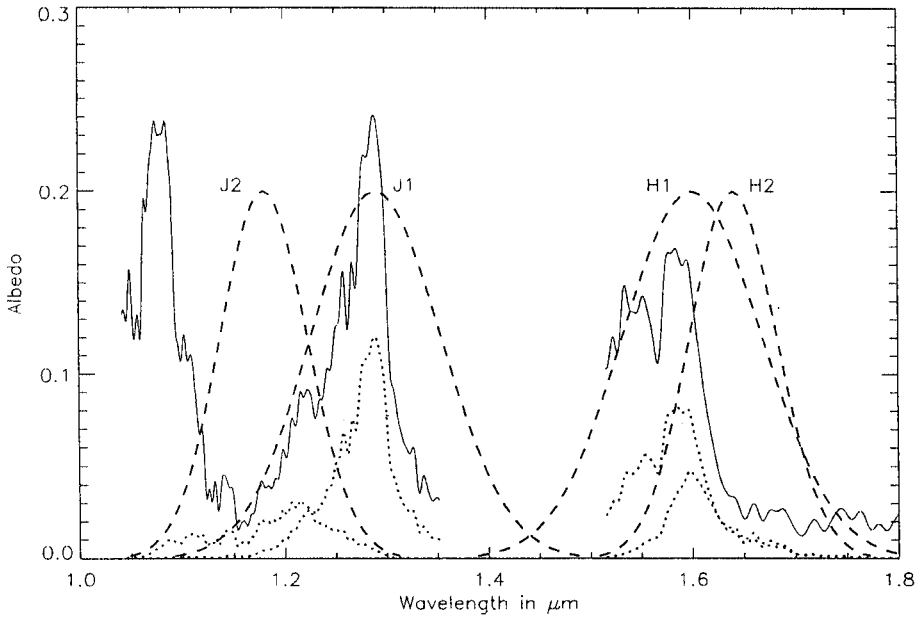

FIG. 1. The J1, J2, H1, and H2 narrowband filters (dashed lines) and their position with respect to the methane windows in Titan's atmosphere, represented by spectra (full lines) from Coustenis *et al*. (1995). The dotted lines were obtained by multiplying the Titan spectra with the profiles of the filters used in our imaging. In the case of the atmospheric images, the maximum flux is displaced with respect to the filters' center, by $+0.04\,\mu$m for J2 and $-0.045\,\mu$m for H2.

and therefore the recovered PSF is very accurate, especially for bright objects such as Titan.

The retrieved resolution on our images is on the order of 0.1 arcsec in H and 0.08 in J, translating into about 10 independent resolution elements or 20 pixels on the disk for the raw images (Table III). Our high-resolution raw images in the J and H bands are shown in Fig. 2 along with the diffraction-limited PSFs, which carried a very high signal-to-noise ratio. The associated Strehl ratios were quite good, about 30–35% in J and 45–50% in H (Table III).

2.4. Orientation of the Images and Longitude Notation

There are two orientation conventions that are usually used in the various papers related to spatialy resolved images of Titan: the astronomical convention with north up and east-sky to the left of north and the cartographic—or geographic—convention with north up and east-map to the right of north. Both conventions are identical in the projections of the images. They differ only in wording. HST papers (Smith *et al*. 1996; Meier *et al*. 2000) and Combes *et al*. (1997a) use the cartographic description, whereas Gibbard *et al*. (1999) use the astronomical one.

TABLE III
Characteristics of the Point Spread Functions

Filter–quadrant	Wavelength (μm)	Strehl ratio	FWHM (arcsec)
J1–C1	1.293	0.313	0.085
J1–C3	1.293	0.354	0.084
J2–C1	1.18	0.289	0.078
J2–C3	1.18	0.320	0.078
H1–C1	1.59	0.460	0.098
H1–C3	1.59	0.491	0.097
H2–C1	1.636	0.459	0.100
H2–C3	1.636	0.438	0.100

Given Titan's synchronous rotation, the sub-Saturn point is fixed and Titan's rotations around itself and around Saturn are counterclockwise when seen from the north. The sub-Saturn meridian is used by all of the authors as the origin of longitudes ($L = 0^\circ$). Then the Titan leading hemisphere is always facing Earth at GEE and the trailing hemisphere at greatest western elongation (GWE). The morning limb is then the anti-Saturn (west-map, east-sky) one at GEE and the sub-Saturn (west-map, east-sky) at GWE.

In articles dealing with Titan spectra, the longitude of central meridian (LCM) convention is always used and hence there is no confusion. The reports of the authors dealing with Titan images differ mainly in longitude notations. HST articles (Smith *et al*. 1996; Meier *et al*. 2000) used geographical longitudes, with their maps centered at $L = 180^\circ$ and east-map longitudes increasing to the right and west-map longitudes increasing to the left, the latter noted L° (W) or $-L^\circ$.

On the Gibbard *et al*. (1999) images, longitudes increase toward east-sky (to the left of north), with the reported dark regions at longitudes of 150–160° (S. E. Gibbard, private communication, 1997), which is the same as using the LCM system (with longitude increasing toward the west-map according to the IAU cartographic convention) as Combes *et al*. (1997a) did. Similarly to the latter authors, in this paper we use the cartographic

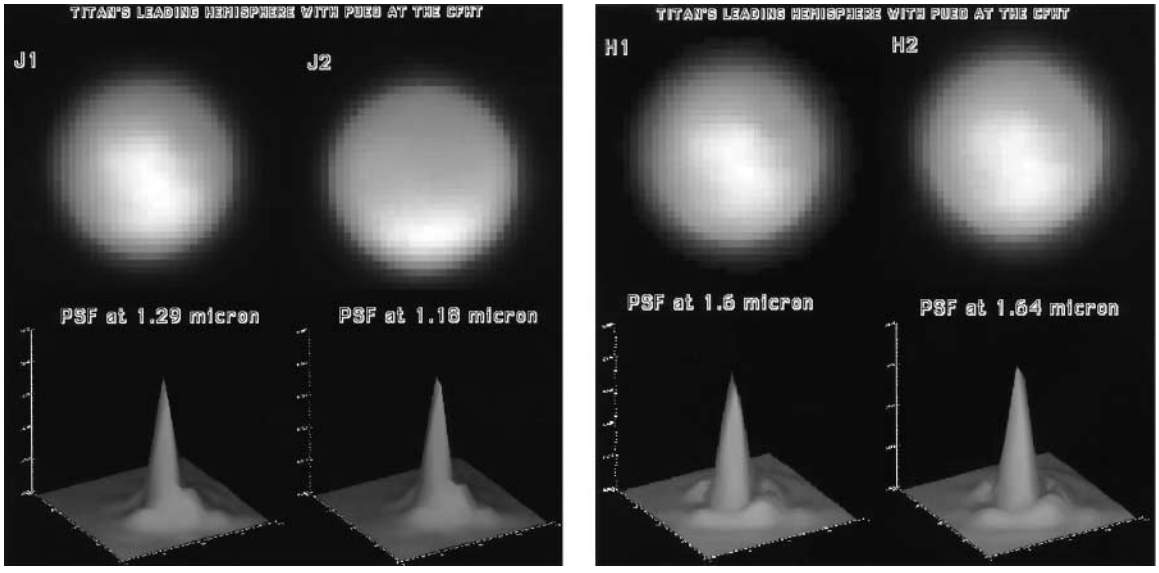

FIG. 2. Raw images of Titan taken at 1.29 (J1) and 1.18 (J2) μm, as well as at 1.6 (H1) and 1.64 (H2) μm with PU'EO, along with the associated PSFs, in surface representations, clearly showing the Airy rings, indicative of achieving the diffraction limit. In the figures containing Titan images, north is up and east-map is to the right (see Section 2.3 for explanations on the conventions).

convention (north up and east-map to the right of north) and the LCM system.

Note that the cylindrical projection maps and/or orthographic projection hemispheric images published by the four teams are very similar and hence in agreement (e.g., Fig. 7 of Combes *et al*. 1997a), with bright and darks spots seen on the same locations and rotating at the same rate from west-map to east-map. This was confirmed between this paper's images and HST images (Smith *et al*. 1996) on a map projection (R. D. Lorenz, private communication, 2000). For further information and to view some explicative images associated with this subject, the reader is invited to visit our Web site (http://despa.obspm.fr/planeto/titan_oa.html).

3. DATA PROCESSING

We have carefully applied sophisticated reduction processes to our data. The elementary images were first corrected for the sky contribution by subtracting the images recorded in the detector quadrant after a Titan pose and while Titan is being recorded in the adjacent quadrant (that is, we record Titan in C1, then in C3 while the sky is recorded in quadrant C1). This method of interleaving Titan and sky elementary exposures is very efficient since the sky brightness in the near-infrared is known to vary rapidly. The elementary images of each quadrant are then co-added, with the sky brightness subtracted, resulting in two Titan images (from C1 and C3). These are then flat-fielded and corrected for bad pixels and correlated noise. The deconvolution and center-to-limb effects processes are applied to each quadrant image separately. To enhance the signal we then sum the quadrants.

3.1. Deconvolution

Thanks to the high quality of the retrieved PSFs and to the high SNR of the images of Titan, the applied deconvolution processes were very efficient. After first tests with well-known methods such as Lucy–Richardson and Wiener, we have also used two newly developed methods that tend to minimize the ringing effects usually associated with the restoration of objects with sharp edges such as planets.

The first of these two methods is the so-called MCS or Magain method (Magain *et al*. 1998). In brief, this method is a two-step process: first the PSF is deconvolved by a kernel function; second the image is deconvolved by the kernel-deconvolved PSF. For both deconvolutions, we used the Lucy–Richardson method, which preserves positivity. The final image has a resolution set by the kernel, which in this case was chosen to be a Gaussian with a FWHM equal to the FWHM of the diffraction figure of the telescope. This significantly reduces the ringing artifacts, which, with more conventional methods, appear near the edge of the planet and prevent accurate photometric measurements.

The last deconvolution method we have applied to our images of Titan is called MISTRAL for Myopic Iterative and STep-preserving Restoration ALgorithm (Conan *et al*. 1998a,b). This method has been especially designed for planetary objects; it is also possible to cope with an imperfectly known PSF (hence the term "myopic"), as explained below.

We have found experimentally that with this last method the ringing artifacts are further reduced while the contrast on the surface is further enhanced. This is probably due to the fact that MISTRAL is a regularized deconvolution method, where the regularization takes *explicitly* into account the presence of sharp discontinuities, without sacrificing resolution to ringing

reduction. By avoiding the ringing effects, it is possible to preserve the initial photometry. Therefore all further deconvolutions in this article will be performed with MISTRAL, which we describe hereafter in more detail.

This method is based on a maximum *a posteriori* (MAP) approach, which means that the restored object is defined as the most likely one given the image, the noise model, and the available prior information on the type of object being observed. By using Bayes' rule and taking the opposite of the logarithm of the probabilities involved, the restored object can equivalently be defined as the one that minimizes a compound criterion, which has two terms. The first term uses a statistical noise model to measure the discrepancy between the recorded image and the image model. Our noise model incorporates both Poisson and detector noises. The second term is the so-called regularization criterion and is a metric in charge of penalizing the objects that deviate from our prior information on the type of object being observed. The prior information used by MISTRAL is that the object consists of a mixture of smooth areas and abrupt edges. The corresponding metric is a so-called $L2-L1$ criterion, which is quadratic for small object gradients in order to smooth out the noise, and linear for large ones; the underlying idea is to smooth out small intensity fluctuations that result from noise while preserving large intensity fluctuations corresponding to the edge of the planet (Conan *et al.* 1998a,b). In the case of the Titan atmosphere, this would translate into a sharp edge of a size smaller than one resolution element, which is the case after the MISTRAL deconvolution was applied to our images (Fig. 3). Additionally, the compound criterion can be shown to be convex, so that the solution is both unique and stable with respect to noise. The minimization of the criterion is performed by means of a fast conjugate gradient routine.

Lastly, MISTRAL also includes a myopic mode for the case of an imperfectly known PSF (e.g., for a PSF obtained by imaging a nearby star shortly before or after the object of interest). In this mode, the object and the PSF are jointly estimated using the above-mentioned information on the noise and on the type of object, as well as the available information on the PSF average and variability; the latter is embodied by an additional term in the criterion to be minimized. The myopic mode is not used in this paper due to the high quality of our PSFs.

To illustrate the results on our Titan images when using the different deconvolution methods, we show on Fig. 3 the J1 and J2 images treated with the Lucy-Richardson, Wiener, Magain, and MISTRAL deconvolutions. All deconvolved images show the same broad features independently of the method used. This gives us confidence in these features, which do not correspond to artifacts. The quality recovered is, however, not the same for each method. In the case of Lucy–Richardson, there are obvious ringing effects, the bright and dark rings clearly seen around the outer parts of the disk. The Wiener deconvolution offers no conservation of positivity for photometry. Here the black outer ring is also followed by a bright edge ring, while a second bright inner ring can be seen in J2. The Magain method shows no evidence for ringing effects, but does not conserve the sharp edges. Finally, MISTRAL preserves the positivity for photometry and the sharp edges and shows no ringing.

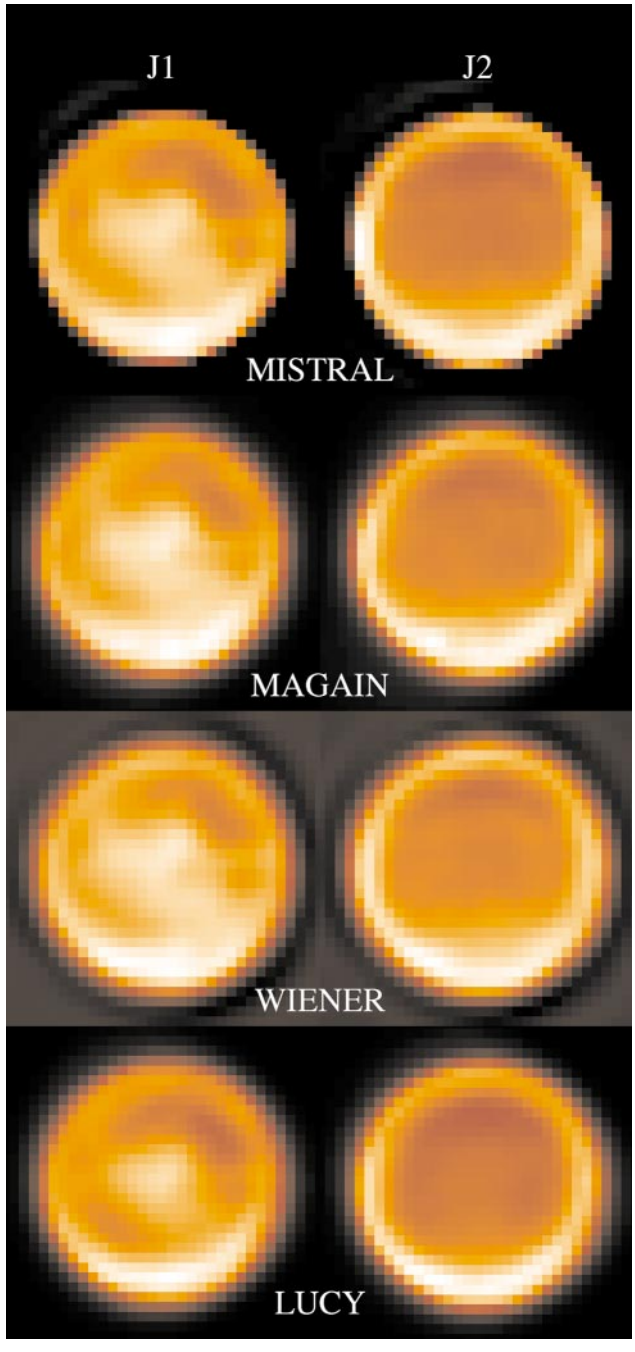

FIG. 3. Four deconvolution methods applied to the J1 and J2 images of Titan. The Lucy–Richardson and Wiener methods are compared to the MISTRAL and Magain methods, which give access to photometry, by preserving the positivity (see text) and show no ringing effects, which are apparent in the images treated by the two classic methods. The MISTRAL method further preserves the sharp edges.

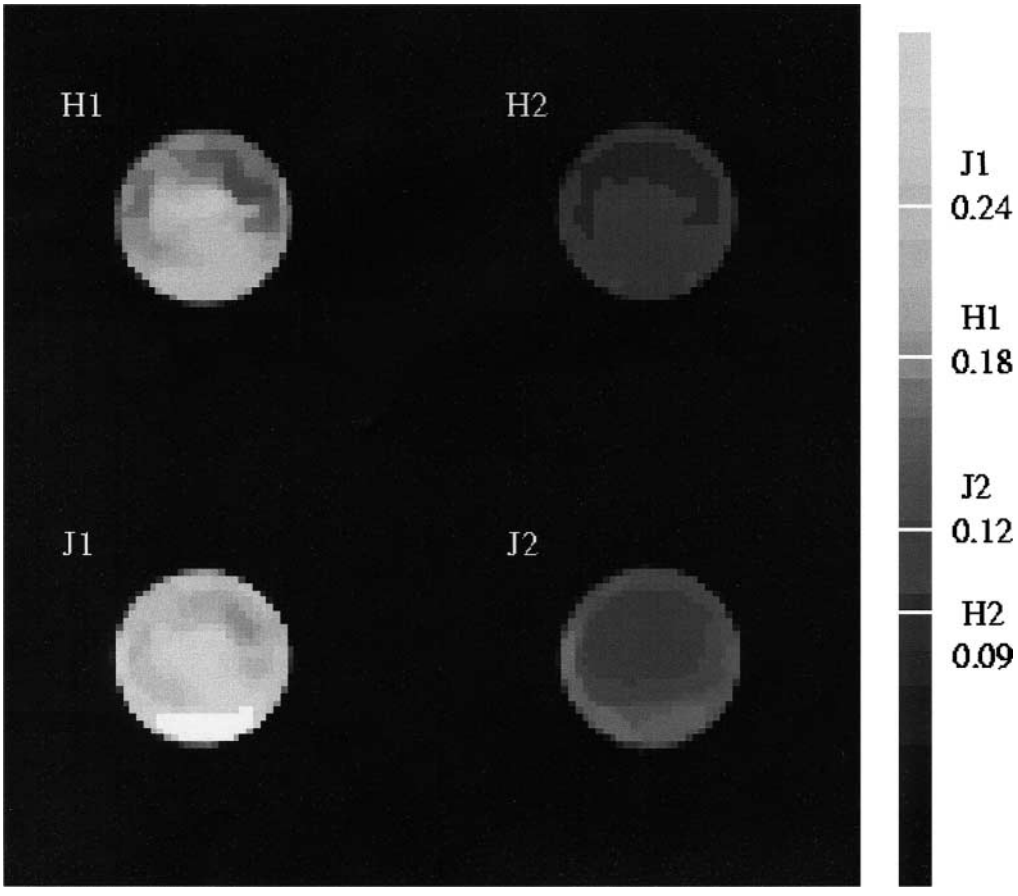

FIG. 4. Titan's geometric albedo maps in the H1 (1.60 μm), H2 (1.64 μm), J1 (1.29 μm), and J2 (1.18 μm) filters, produced from the images deconvolved with MISTRAL.

Following deconvolution the center-to-limb effects have also been modeled, taking into account the fractal characterization of the Titan aerosols (Rannou *et al*. 1999), and the appropriate correction was applied to the images (see Combes *et al*. (1997a) for details). The limb effects are very little influenced by the ringing, and we are clearly in the presence of sharp edges.

3.2. Photometric Calibration: Titan's Geometric Albedo

We have calibrated the solar flux incident on Titan in each of our images (after deconvolution but without center-to-limb effects correction). We do so by multiplying it with Gaussians simulating the filters' effects at the associated wavelength (Fig. 1) and defined the photon flux from the atmosphere for each filter, hence the specific radiation intensity. For this we have used interleaving observations of a standard calibration star (see Table I): HD152274 is a F5-type star ($\alpha = 2\text{h}27'45''$, $\delta = 8°51'30''$) of magnitude 8.49 in J and 8.276 in H.

The absolute photometric accuracy on our images is better than ~5%. The MISTRAL algorithm we used for the deconvolution effectively preserves the total flux. Taking into account the image processing and the flux calibration, our albedo values are good to ~10%.

We have then obtained albedo maps for each deconvolved Titan image (Fig. 4), where the disk averages represent the geometric albedos, equal to 0.24, 0.12, 0.18, and 0.09 for J1, J2, H1, and H2 respectively (Table II), in good agreement with spectroscopic measurements of Titan's geometric albedo at these frequencies (Lemmon *et al*. 1995; Coustenis *et al*. 1995; Griffith *et al*. 1998).

4. FEATURES OBSERVED

In the J2 filter we are sounding the upper atmosphere since, due to the strong CH_4 absorption at 1.18 μm, the contribution to the signal from the surface and the lower atmosphere is definitely negligible. This is also basically the case for the H2 filter, even if its characteristics are not as favorable as expected. This is all the more the case closer to the planet's limb and away from the image center, in all filters, including J1 and H1. The latter two filters (and to a lesser extent H2) show additional bright areas and darker inlets (mainly close to the center), due to the surface and to some contribution from the lower atmosphere. Because some of these features (like the central bright spot) were observed at different times by various investigators and they recur without

changing position or shape, it is highly probable that they are not transient phenomena (such as moving clouds), but real surface morphology.

The features observed in our images and pertaining either to the atmosphere or to the surface (insofar as we can distinguish the two components) are discussed extensively hereafter.

4.1. Titan's Atmosphere

Two phenomena can be observed in the J2 deconvolved images (Fig. 3) and on the photometric profiles (Fig. 5): a quite extended north–south asymmetry and a west–east (or morning/evening) asymmetry restricted to the limbs.

Vertical and horizontal profiles of our deconvolved images at the four spectral bands are shown in Fig. 5. All the filters clearly show the north–south atmospheric asymmetry, with a bright south polar region extending over 4 pixels and corresponding to a brightness increase of about 17–33% in the south with respect to the north. This phenomenon has been previously observed by Caldwell *et al*. (1992), Combes *et al*. (1997a), and Gibbard *et al*. (1999). It is not present in the final results published by Smith *et al*. (1996) or Meier *et al*. (2000) due to the data reduction method applied to the HST images and which tends to eliminate zonally symmetric surface features, as pointed out by the authors. It is observed, however, clearly on their published raw data before subtraction of a "mean atmosphere." This asymmetry has been extensively discussed in previous papers, and is attributed to seasonal effects on Titan (see for instance Lorenz *et al*. (1997)), associated with a strong seasonal enhancement of the haze optical depth in the south polar region (the reverse was true during the *Voyager* encounter). In Combes *et al*. (1997a), this enhancement of opacity over Titan's south pole was evaluated to be of about twice the northern opacity.

Another feature, of an origin different than the previous one, which significantly shows in our J1 and J2 images (about 9% in J1 and 16% in J2 and at levels of $<5\%$ in H1 and H2), is a brightness increase on the morning limb (west-map) of Titan (Figs. 3, 5, 6). A bright feature is indeed observed over 2 pixels on the anti-Saturn side of Titan during greatest eastern elongation. This feature was not observed in the ADONIS images at 2 μm, and, to our knowledge, there is no previous report for it in other investigations, although there may be some indication for it in a recent presentation of Keck images (Roe *et al*. 2000). Because ringing effects are significantly reduced in our images, this feature is clearly distinguishable as a real component of Titan's atmosphere. Some hints as to the possible origin of the second effect are given in the discussion.

4.2. Titan's Surface

We have applied the MISTRAL deconvolution and center-to-limb effects treatment to our J1, J2, H1, and H2 images, shown in Fig. 6. We have then subtracted a fraction of the J2 and H2 images from the J1 and H1 ones respectively, so as to eliminate the atmospheric contribution and recover the surface morphology, as was done in Combes *et al*. (1997a).

The images of Titan's surface resulting from J1-kJ2 and H1-k'H2 subtractions (where $k = 0.5$ and $k' = 0.6$, see Combes *et al*. (1997a) for more details on these factors, estimated from the filters' transmission and exposure times) are shown in the lower part of Fig. 6 and in Fig. 7 with a spherical grid superimposed. Titan's central longitude is close to 90°E. The contrast we achieve is of the highest reported at these wavelengths, namely 30–40%. This allows us to clearly resolve the bright complex region extending from roughly 70° to 120° LCM close to equatorial latitudes. It is shown to consist of at least three individual peaks that are about 15–20% brighter than the surrounding areas in both wavelengths, as was also found at 2 μm in the ADONIS images.

Our surface brightness contoured images, produced for a normalized value of 1 at the brightest spot in J and H, are shown in Fig. 8. From this figure it appears that the central bright equatorial region is about three times brighter than the darker areas in both J and H. Bright extents are also observed in the north–west and south–east regions. Furthermore, we resolve the somewhat darker mideastern (−20°, 50° LCM) and southwestern (−40°, 130° LCM) inlets extending symmetricaly on each side of the lower bright spot. There are other darker terrains to be found in our images at western longitudes (vertical and close to the edge), and in northeastern locations, at longitudes of about 40°–70° LCM, extending from the equator to about 30°N with relative brightness in the range 0.2–0.4. If the averaged surface reflectance in these images was normalized to the albedo values inferred for the leading hemisphere by Coustenis *et al*. (1995) and Lemmon *et al*. (1995), i.e., 0.4–0.6 in J and 0.4–0.5 in H, the bright spot would be associated with isocontours of about 0.9 and 0.7 (in J and H respectively) and the darker areas would have albedos of 0.2–0.3. In this case, these regions would not appear as "black" as those reported in Gibbard *et al*. (1999), which are however located in a different part of the Titan disk, near 150°–160° LCM, at the edge of our own images. However, given the discrepancy among the reported values for Titan's surface albedo and given the uncertainties still attached to the treatment of the atmospheric component (whether by image subtraction or by modeling), we believe that it is not currently possible to infer any reliable surface albedo map for Titan and hence we restrain ourselves to the relative contrast information given in Fig. 8.

From the comparison of our 1.3- and 1.6-μm images with the ADONIS 2-μm images (see Fig. 5 of Combes *et al*. (1997a)), it appears that the same surface morphology is observed, with the bright spot and the darker areas exhibiting similar contrasts at all three wavelengths.

5. DISCUSSION

All of our images show Titan's southern limb brighter than the northern one. This phenomenon is related to seasonal effects, resulting in the enhancement of aerosols in the south pole of

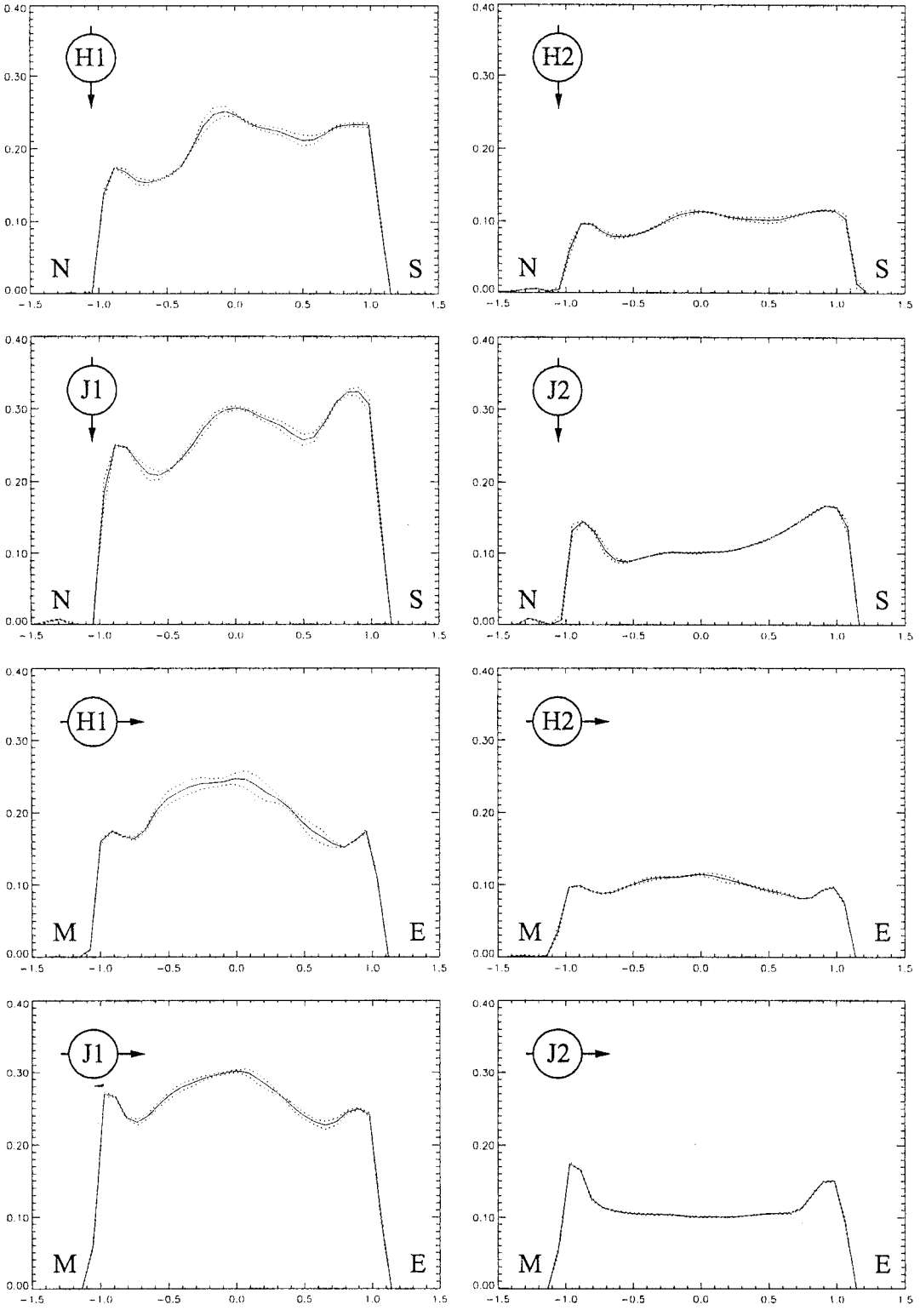

FIG. 5. Profiles of Titan's atmospheric albedo. North–south (four upper figures) and morning (west-map)–evening (east-map) (four lower curves) profiles are shown for J1, J2, H1, and H2. On the ordinate axis, zero is the center of Titan's disk, and on the coordinate axis the profile is measured in units of Titan's radius. The enclosing curves (dotted lines) correspond to the deviation of the brightness over ± 3 pixels. The uncertainty on the inferred N/S and M/E ratios is about 5%. The N/S asymmetry varies from 17 to 33% depending on the filter, whereas the M/E brightness is clearly observed (above the 5% error bar) in the J1 images (+9%) and in the J2 images (+16%).

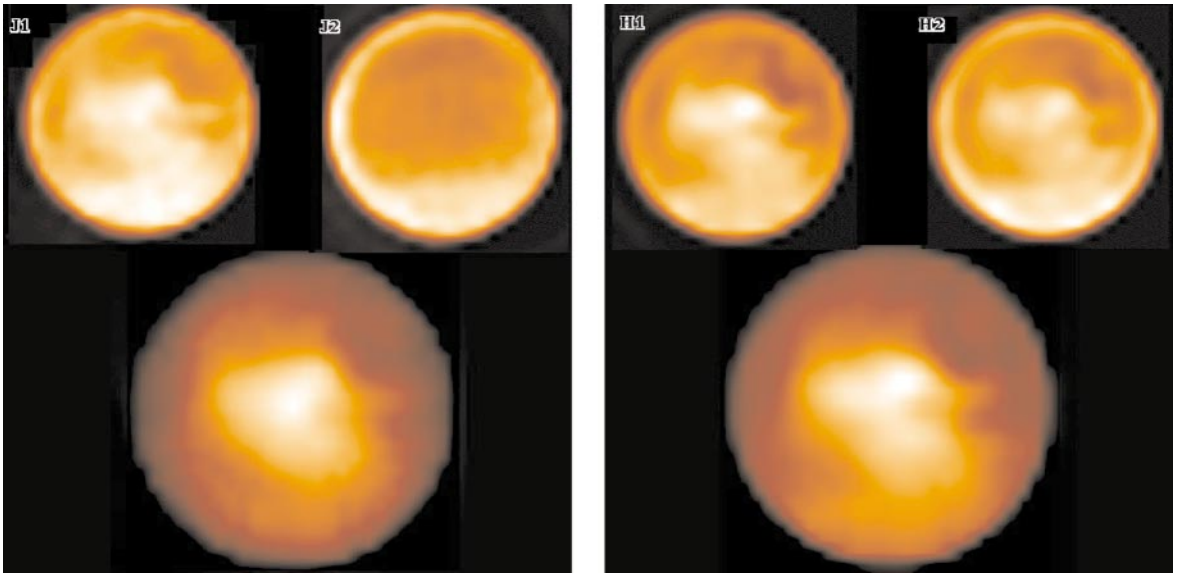

FIG. 6. Correction for limb effects was applied to the J1, J2, H1, and H2 deconvolved images of Titan. The images were smoothed. In order to dispense with the atmospheric contribution, we performed the subtractions J1-kJ2 and H1-k'H2 (see text). The resulting images of Titan's surface are shown at 1.3 and 1.6 μm.

Titan. In almost all of our filters also, the morning side (that is, the side coming out of the night) is consistently brighter than the evening side. As shown before, the deconvolution ringing effect is minimized and can be neglected. As mentioned in Section 2.2, the phase angle effect on our images would be a bright evening limb, not a morning one. We therefore are quite confident that our bright limb feature is not due to phase effects. There may be other aspects that could contribute to this phenomenon that we do not see at present, but we think that our suggestion of meteorology (through the possible presence of a morning fog) on Titan is valid.

Nevertheless, a very narrow (spatially resolved and showing in less than 2 pixels) bright ring is expected all around the satellite due to backscattering in the stratosphere. Brightness variations in this ringlet should be linked to variations in the stratospheric aerosols density. These differences are probably diurnal effects, linked to the geometry pertaining to the Sun rather than to Saturn. We suggest that they are due to meteorology effects in Titan's stratosphere.

In order to investigate these phenomena we use our haze model (Rannou *et al*. 2001) and the methane absorption coefficients from sources as reported in Coustenis *et al*. (1995): 0.02,

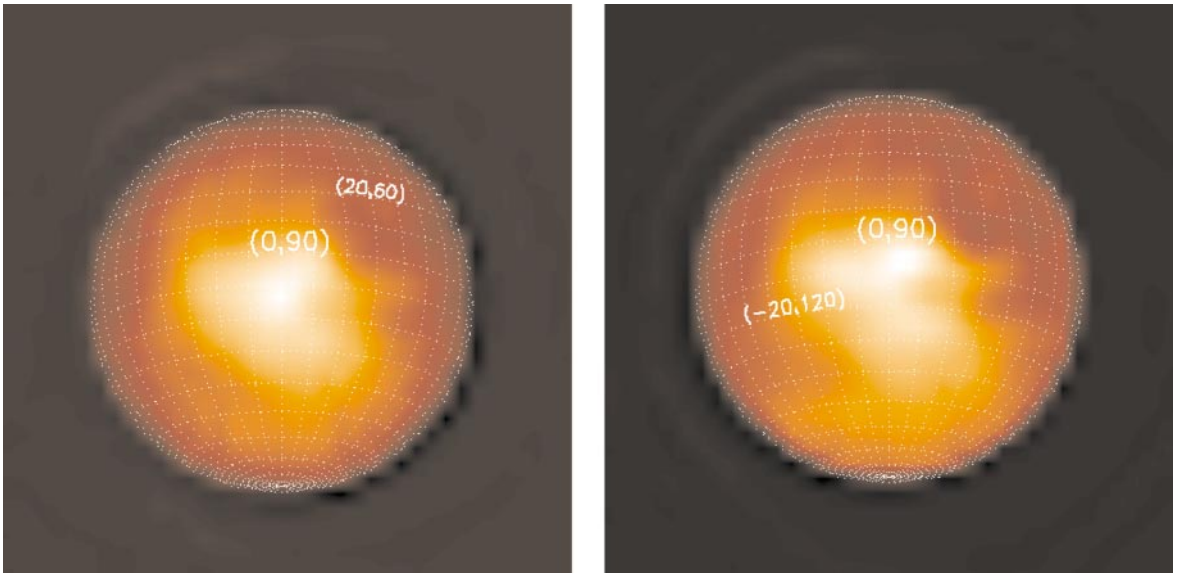

FIG. 7. Spherical grids superimposed on Titan's smoothed surface images of the leading hemisphere at 1.3 (left) and 1.6 (right) μm. The equator is marked by the (0, 90) degrees point. According to the IAU convention, longitudes increase toward west-map, to the left here. The subsolar latitude and longitude points on the date of the observations were -15.5° and 92° respectively. Two other points of (lat, lon) are given to help the reader locate the various areas discussed in the text.

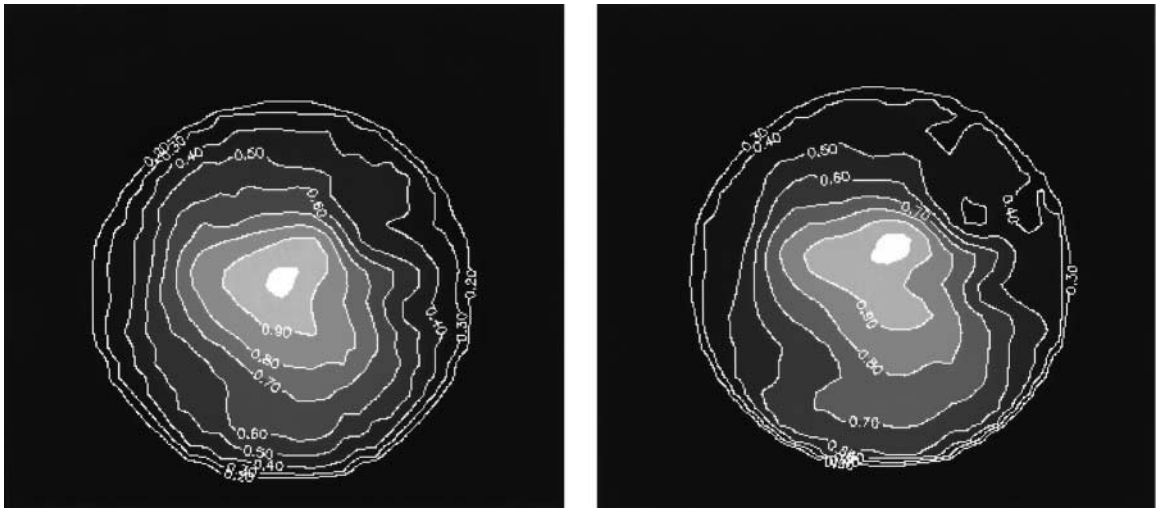

FIG. 8. Contoured profiles of the relative surface brightness on the subtracted images of Titan's surface at 1.3 μm (left) and 1.6 μm (right). The brightest area close to the center was normalized to 1. There is a factor of ~3 difference in surface reflectivity between the bright equatorial spot and the darker peripheral areas.

6.5, 0.02, and 0.1 (km-am)$^{-1}$ for J1, J2, H1, and H2 respectively. We set the methane saturation rate to $S = 1$ in the troposphere. This gives 1.8% of methane in the troposphere. Figure 9 shows the atmospheric altitude probed at the four wavelengths discussed in this paper, and for different viewing geometry conditions. The two additional wavelengths correspond to the filters K1 and K2 used with ADONIS, and are given for information. From this figure we note that the H1, H2, and J1 filters allow us to sense Titan's low atmosphere and the surface, whereas the J2 filter essentially senses above 50 km. The center of the image reflects mainly the surface, through the atmosphere, and at the limb basically only the atmosphere contributes to the reflected light. The left part of Fig. 10 shows that we can reproduce the north–south profile of our J2 images with a relatively small haze optical depth (0.18–0.38), but with the requirement of having about twice more haze in the south than in the north (in agreement with findings by Combes *et al*. (1997a) and Gibbard *et al*. (1999)).

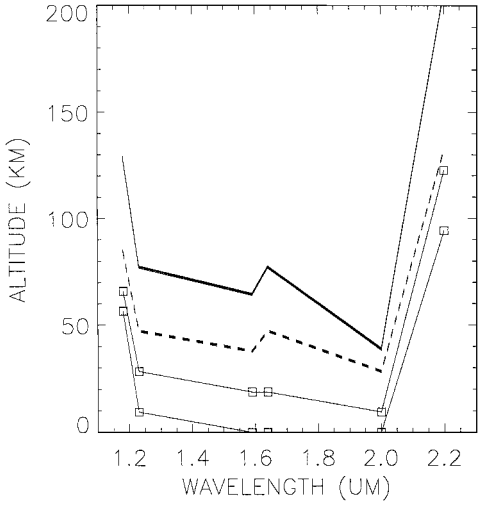

FIG. 9. The altitude, Z^*, probed in Titan's atmosphere at the six wavelengths corresponding to the filters J2, J1, H1, H2 (in this paper) and K1 and K2 (in Combes *et al*. 1997a). The linked squares correspond to a normal solar incidence (lower curve) and an incidence of 60° (upper curve) in a spherical shell atmosphere. The heavy dashed line shows the altitude Z^* at the limb of the planet. The solid heavy line shows Titan's optical radius (tangential $\tau = 1$). Note that the altitude Z^* is primarily controlled by the methane absorption and not by the haze, which rather determines the albedo value.

5.1. Interpretation of the W/E Limb Asymmetry

A haze model that works for the north/south asymmetry is used also in the case of the morning/evening feature.

5.1.1. Constraints on the altitude. In order to estimate the altitude where this morning-limb brightening occurs, we use the information from Fig. 9. Because the atmosphere is clear, only the extreme part of the limb really senses the stratosphere in H1, H2, and J1. In the J2 image, only the atmosphere contributes to the reflected light, because due to the methane absorption, the light is stopped at high altitudes. This explains the general shape of the images, with a somewhat flat center and with a sharp increase in reflected light seen at the limb. Because the W/E asymmetry shows up better in the J2 images than in the H1, H2, and J1 images we infer that the J2 filter really senses the region where the change in atmospheric properties occurs. Two such changes must occur: first, the sharp bright limb implies that there exists a level below which the atmosphere or the surface appears dark and above which the atmosphere is suddenly bright. This may be due to a change in the haze properties. Secondly, the W/E asymmetry indicates that the atmospheric properties are not the same at the two limbs.

Figure 9 indicates that the sharp change in scattering properties must occur preferentially at an altitude between 70 and 100 km. The reason is that the J2 filter probes near 70 km for a

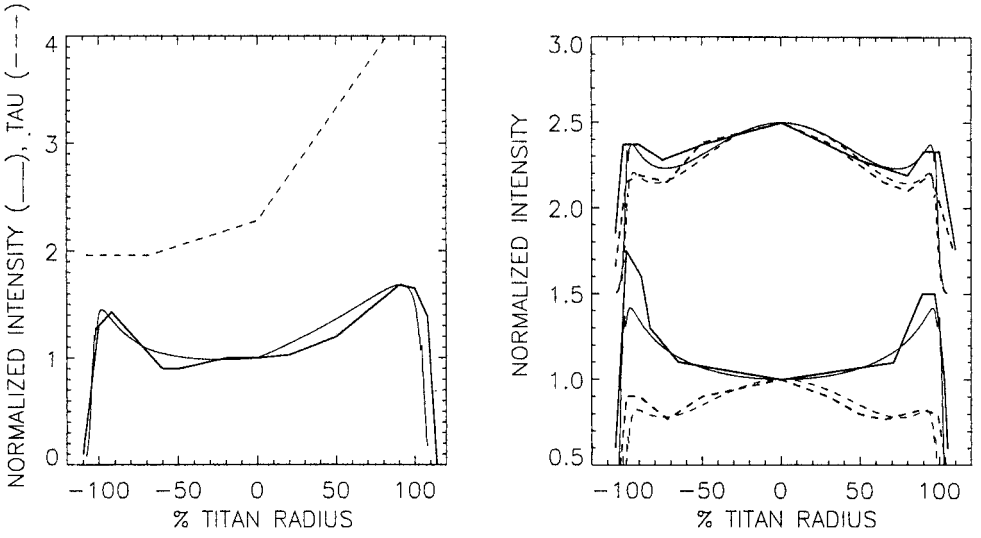

FIG. 10. (left) Model fits for the J2 north/south (left to right) image cuts (heavy solid line). The model is the light solid line. The haze optical depth (multiplied by 10 for clarity) is shown by the dashed line. (right) Morning–evening (or west-map to east-map) relative profiles (heavy lines) taken from Fig. 5 are fitted with synthetic profiles (light curves). The lower curves are for J2 (solid line) and J1 (dashed line), the upper curves are for H2 (solid line) and H1 (dashed line) and are shifted by +1.5 for clarity. The centers of the J1, H1, and H2 images probe the troposphere and surface, whereas the limb of these images and J2 probe the stratosphere.

solar incidence angle of 60°, and near 100 km at the limb. The asymmetry should be due to differences in the haze properties at these altitudes. From Fig. 9 we can also predict a similar effect in the K2 filter, which probes atmospheric levels around 90 to 130 km. Thus, information from the K2 filter would bring very important constraints on the vertical extent of the limb asymmetry. Our fits of the west-to-east profiles of our images are shown in the right half of Fig. 10.

5.1.2. Physical interpretation. Constraints on the vertical structure of the haze exist. Microphysical models associated with a radiative transfer code allow one to model the Titan geometric albedo. Models using fractal aggregates must include a cutoff in the haze distribution to produce a correct fit (Tomasko *et al.* 1997; Rannou *et al.* 2001). The cutoff must be applied somewhere between 70 and 120 km. Rannou *et al.* (2001) show that the removal may be produced by the collection of material (coagulation or condensation) consistent with liquid hydrocarbons, but not with photochemical polymers. Moreover, they find that the drops produced must have radii of around 1 μm.

The altitude range and the available quantity of material required to build the drops are fully consistent with the condensation of methane byproducts such as ethane and acetylene (the most abundant), with mass fluxes estimated to be 50 to 100 times the aerosol mass flux (Yung *et al.* 1984).

Thus, a straightforward interpretation of the observed morning/evening asymmetry, located at altitudes in the range 70 to 90 km, is to assume that we are sensing the diurnal condensation cycle of condensable species. One Titan night lasts 8 terrestrial days. Even considering winds of 50 m/s at 10 mbar (Hourdin *et al.* 1995), the atmosphere resides in the dark side for about 1.5 terrestrial days. The drop in temperature, while small, may be sufficient to enhance the condensation on the cold morning limb with respect to the warm evening limb. The nucleation and condensation physics are very sensitive to the temperature, and a gap of a few kelvins may generate large optical effects. However, this scenario should be studied in detail using a thermal model coupled with a cloud microphysical model. This is beyond the scope of this paper. The purpose of this short analysis of the data is to present the only consistent information that it is possible to infer from these images, that is, the altitude where this phenomenon occurs. Currently, further characterization of the clouds from this data only is difficult to impossible. Thus, we consider that the information about the morning-to-evening side asymmetry is essentially qualitative. On the other hand, the altitude where it occurs essentially depends on the atmosphere opacity due to methane; thus it can be determined precisely. The haze (and possibly cloud) opacity is also involved in the brightness (or albedo) values, but depends on too many parameters that cannot be constrained here.

To conclude, we stress that we may be seeing in our data the first diurnal effect ever observed on Titan, in the possible presence of a morning fog. The altitude of the asymmetry source is estimated to be around 70 to 90 km, which is consistent with condensation of species such as ethane and ethylene. The morning/evening asymmetry could be due to a temperature difference. The morning limb coming out from the night period should be colder than the evening limb just leaving the dayside. The *Voyager* RSS data show an evening temperature (egress) that is lower than the morning temperature (ingress) by 2 to 3 K (Lindal *et al.* 1983). This is the opposite of what would be expected, because from basic arguments we would expect a drop

in the temperature in absence of sunlight during the night. However, the egress and ingress profiles correspond to latitudes of 6.2°N and 8.5°S. The temperature difference could be attributed to the 15° latitude difference rather than to the hour of the day. Another possibility is that the temperature difference actually corresponds to a refractivity difference between the morning side and the evening side. The occultation equation actually shows that $d(\ln T)/dz + mg/kT = -d(\ln(n))/dz$, where n is the refractive index of the atmosphere, m the mean molecular weight, k the Boltzman constant, g the gravity, and T the temperature. By rearranging the equation, one can show that an excess of refractive index between the two sides, due to different condensible species or clouds, can easily be interpreted as an excess in temperature. One finds that the atmospheric density at 100 km (10 Pa) is about 1.5×10^{-4} kg/m^3. A cloud could represent a nonnegligible fraction of the total atmospheric mass; a cloud of 50 km in thickness, having 1% of the atmospheric mass at each level, would only represent 75 g/m^2. Such a cloud could lead to a bias in the refractive index and thus in the temperature determination. In Lindal *et al*. (1983) only one refractive species (molecular nitrogen) was considered for both sides, and the authors directly converted the refractivity in terms of a pressure profile. Depending on the induced effect of potential clouds or secondary species at 3.6 and 13 cm of wavelength, the truth could be slightly different. We consider that this point could be a potential clue for clouds and it deserves to be considered in a specific study. We note that Lindal *et al*. 1983 do not comment on this difference between the two sides, and in the absence of more information, it is difficult to take this matter any further in this paper.

Thus and before we can firmly identify the source of this second atmospheric phenomenon we need to observe it again and to further investigate its behavior as a function of wavelength (by moving to even shorter frequencies, at 0.94 and 1.1 μm, and to longer ones near 2 μm) and of orbital phase (by observing the anti-Saturn hemisphere of Titan and by exploring the appearance of the morning/evening feature during GWE).

5.2. *Plausible Surface Candidates*

The large equatorial region on Titan appears bright at the three wavelengths (1.3, 1.6, and 2 μm) investigated by adaptive optics (both with PU'EO and ADONIS) by this group, and at the additional shorter wavelengths (0.94 and 1.1 μm) observed by the HST (Smith *et al*. 1996; Meier *et al*. 2000). Some of the brightness associated with this feature could be due to near-surface haze/cloud opacity, like orographic clouds connected to topography. Our J1-*k*J2 subtraction is in this respect more sensitive to localized near-surface atmospheric opacity than the zonal average approach used with the HST data. However, even in this case, the presence of an additional brightening component (ice and/or relief) is required to explain the factor of 3 difference in albedo between the bright and dark terrain (Coustenis *et al*. 1995). The fact that the bright equatorial region persists at all covered wavelengths so far argues against its being covered with water ice, the latter strongly absorbing at 2 μm and to a lesser extent at 1.6 μm, at which wavelengths, it should therefore appear darker. Other plausible candidates include CH_4 (and other hydrocarbons), NH_3, and CO_2 (Griffith *et al*. 1991). Evidence for CO_2 was not found in ADONIS CVF images around 2 μm (Combes *et al*. 1997b). Neither was there any indication of NH_3. Hydrocarbon (methane or ethane for instance) frost has no absorption bands at the three considered wavelengths or at the shorter ones (Schmitt *et al*. 1998; Quirico and Schmitt 1997), and would then appear bright in the Titan images.

There are two questions at this point: (a) why would the bright equatorial area be different than the surrounding terrain, if it was just a matter of constituents? (b) Can methane ice exist on Titan's surface?

For the equatorial bright region to be different than the rest of the Titan disk, a reasonable assumption would be that it is related to some topography (relief). Coustenis *et al*. (1997) have investigated the presence of a mountain that could explain the dark vs bright appearance on Titan. They concluded that a mountain (of any reasonable size) by itself is not enough to explain the total brightness variation between the leading and the trailing hemisphere. The mountain would cause some brightness by virtue of simply having the light reflected through less methane absorption at higher altitudes, and the additional bright component would complement the increase in albedo. On the other hand, it is possible to have a combination of a mountain (or crater) and a bright constituent on top of it.

Could this constituent be methane ice? Given the current uncertainties on the methane atmospheric abundance, and on the ground temperatures prevailing on Titan (especially outside the equator or at other seasons than northern spring equinox), we cannot dismiss this possibility.

The surface spectrum retrieved by near-IR spectroscopy with the FTS (Coustenis *et al*. 1995; 1997) show relative albedos of about 0.4–0.7 in the J and H bands and two times less in the K band. They are even lower at 0.94 μm on a disk-average. This is compatible with the presence of methane (or ethane) frost and water ice on the Titan surface, probably covered by sediments of organics. Tholins are known to be bright in the near-infrared, down to about 1 μm (Khare *et al*. 1984), so they could add to the overall ground brightness. At 0.94 μm, the tholin material would however appear darker than at other wavelengths.

Furthermore, the Titan poles are known to have colder temperatures than the equator, at least in the stratosphere, with the greatest decrease of about 20 K in the north pole at the time of the *Voyager* encounter. Should this situation persist on the ground, and the temperatures be lower than around 90 K at the poles, methane ice could also explain the presence of the bright mid-latitude zones at the poles observed clearly in the ADONIS images of Titan's trailing hemisphere, but which could possibly be present all over the disk (Combes *et al*. 1997a). If these are polar caps, why their extent to the poles is not obvious in the images could simply be a scattering phase function effect (see

a similar case and explanation in the case of Mars in Erard (1991)).

However, simple considerations on the production of solid particles in the Titan atmosphere (e.g., Kouvaris and Flasar (1991); Thompson *et al*. (1992), and Samuelson and Mayo 1997) seem to indicate that in the case of thermodynamical equilibrium with the atmosphere, the particles falling through it would form CH_4-rich (75–86%) snow at total pressures of less than 700 mbar (that is, at altitudes of more than 12–14 km, depending on the authors). This snow would melt at lower altitudes. Figure 3 of Kouvaris and Flasar (1991) well illustrates this transition and shows that if the profile is shifted toward lower temperatures the melting pressure is even lower (all this is related to the form of the solidification curve of the N_2–CH_4 mixtures as a function of temperature and total pressure).

Another possibility is the case of a nonthermodynamical equilibrium (B. Schmitt, 2001, private communication), where the solid particles formed at or above 12–14 km of altitude and could not adjust either their composition or their temperature with that of the atmosphere surrounding them. If, for instance, they preserved their composition as it was at equilibrium at 14 km (that is, 85.3% of CH_4 at 80.6 K, as if they were sensitive only to the temperature and not to the pressure/composition of the atmosphere), their melting temperature would be 85 K. In this case, and for the surface equatorial temperatures of 94 K (Lindal *et al*. 1983), associated with a methane abundance of 12% in the atmosphere, a 6–7-km-high mountain could host a layer of methane-rich ice on its top. Methane could condense and be deposited in the form of more or less clean and fresh snow on the top of a relief. Also, should the temperature or the mountainous plateaus height vary within the bright area, it could explain the existence of higher and lower brightness peaks. Methane snow on a high top would be much more reflective than methane ice on the ground.

However, the case of a nonthermodynamical equilibrium is difficult to defend because it is not realistic. Indeed, as soon as the drops begin to liquefy above 80.6 K, they need to either evaporate the methane or to condense N_2 in order to be in equilibrium with the atmospheric composition (73.8% of CH_4 for a liquid at 80.6 K and raising with temperature). Given the high saturation pressures of CH_4 and N_2 (and hence the high dynamic condensation/evaporation fluxes) and the feeble precipitation velocities for the solid particles (1–2 m/s, Lorenz 1993) there should be enough time for the equilibrium to occur even with particles/drops of several millimeters in size. Furthermore, even if the snow did arrive on the top of a mountain, it could not remain there in a solid form for any long periods of time but would melt promptly.

Another (and perhaps more plausible) possibility for producing a bright material such as snow with the required characteristics is ethane. The solidification temperature of pure C_2H_6 is 89.3 K (this would produce some snow above altitudes of about 3.5 km, if it was pure). Ethane being less volatile (Lunine *et al*. 1983), it is less sensitive to the presence of N_2 and there should then be less nitrogen included in the N_2–C_2H_6 mixtures, and hence the melting temperature should not be much lower than 89 K. These mixtures show a spectral behavior quite compatible with that inferred from our observations (Quirico and Schmitt 1997). Although the spectral characterization of these mixtures is well known (Pearl *et al*. 1991; Schmitt *et al*. 1992; Quirico and Schmitt 1997), there is very little information on the phase diagram of N_2–C_2H_6(–CH_4) at the right temperatures for Titan. On the other hand, the ethane flux estimated from current models for Titan is rather small (on the order of 1 μm per year). Also, ethane being fully miscible with methane and in small quantities, an ethane–methane–nitrogen liquid rather than ethane ice might form. However, the uncertainties in present data are large enough to allow for ethane ice to be a possibility for Titan's bright spots. Perhaps this is something that can be tested by observations. Thus, in the future, it would be useful to compare measurements taken by the HST or other telescopes at the various wavelengths.

6. FUTURE WORK

We need to refine our findings with more modeling and to recover images at 0.94 and 1.08 μm, which we have demonstrated to be feasible with PU'EO. We also need to take more data on the trailing hemisphere, where we have shown a north–south asymmetry to exist, with brighter zones in the north (Combes *et al*. 1997a). In order to identify the source of the western-limb brighteness, we need to observe more with PU'EO and similar systems so as to characterize its behavior as a function of wavelength and orbital phase.

Titan's surface is still a mystery and an exciting place to look at. We have come a long way from the global hydrocarbon ocean that was a common description 10 years ago, but we still have a lot of controversy to overcome about the real nature of the ground. The pieces of the puzzle are, however, coming together little by little and we may be able to go beyond speculation in the near future.

ACKNOWLEDGMENTS

We thank Bernard Schmitt for valuable input on plausible surface candidates. Stéphane Erard, and Emmanuel Lellouch for fruitful discussions about what we are seeing in our images. We thank also Jean-Luc Beuzit and Marie-Claire Hainaut for assistance with the observations.

REFERENCES

Caldwell, J., C. C. Cunningham, D. Antony, H. P. White, E. J. Groth, H. Hasan, K. Noll, P. H. Smith, M. G. Tomasko, and H. A. Weaver 1992. Titan: Evidence for seasonal change—A comparison of Hubble Space Telescope and Voyager images. *Icarus* **96**, 1–9.

Combes, M., L. Vapillon, E. Gendron, A. Coustenis, O. Lai, R. Wittemberg, and R. Sirdey 1997a. Spatially-resolved images of Titan by means of adaptive optics. *Icarus* **129**, 482–497.

Combes, M., A. Coustenis, E. Gendron, L. Vapillon, R. Wittemberg, and J.-P. Véran 1997b. Titan's near-IR imaging with adaptive optics. *Bull. Am. Astron. Soc*. **29**, 1039, Proc. of the 29th Annual Div. of Planetary Sciences Meeting, Cambridge, MA, 28 July–1 August. [Abstract]

Conan, J. M., T. Fusco, L. Mugnier, E. Kersalé, and V. Michau 1998a. Deconvolution of adaptive optics images with imprecise knowledge of the point spread function: Results on astronomical objects. In *Astronomy with Adaptive Optics: Present Results and Future Programs, ESO/OSA Workshop, Sept. 1998, Sonthofen, Germany*.

Conan, J. M., L. M. Mugnier, T. Fusco, V. Michau, and G. Rousset 1998b. Myopic deconvolution of adaptive optics images using object and point spread function power spectra. *Appl. Opt.* **37**, 4614–4622.

Coustenis, A., E. Lellouch, J. P. Maillard, and C. P. McKay 1995. Titan's surface: Composition and variability from its near-infrared albedo. *Icarus* **118**, 87–104.

Coustenis, A., E. Lellouch, M. Combes, R. Wittemberg, C. P. McKay, and J.-P. Maillard 1997. Titan's atmosphere and surface from infrared spectroscopy and imaging. In *Astronomical and Biochemical Origins and the Search for Life in the Universe* (C. B. Cosmovici, S. Bowyer, and D. Werthimer, Eds.), pp. 227–234. Proceedings of IAU Colloquium 161.

Erard, S. 1991. Minéralogie des surfaces de Mars et Phobos: Étude par spectro-imagerie infrarouge en orbite. Ph.D. thesis, Thèse de Doctorat de l'Université Paris VII.

Gendron, E., and P. Léna 1994. Astronomical adaptive optics: I. Modal control optimization. *Astron. Astrophys.* **291**, 337.

Gendron, E., and P. Léna 1995. Astronomical adaptive optics: II. Experimental results of an optimized modal control. *Astron. Astroph. Suppl. Ser.* **111**, 153.

Gibbard, S. E., B. Macintosh, D. Gavel, C. E. Max, I. de Pater, A. M. Ghez, E. F. Young, and C. P. McKay 1999. Titan: High resolution speckle images from the Keck telescope. *Icarus* **139**, 189–201.

Griffith, C. A. 1993. Evidence for surface heterogeneity on Titan. *Nature* **364**, 511–513.

Griffith, C. A., T. Owen, and R. Wagener 1991. Titan's surface and troposphere, investigated with ground-based, near-infrared observations. *Icarus* **93**, 362–378.

Griffith, C. A., T. Owen, G. A. Miller, and T. Geballe 1998. Transient clouds in Titan's lower atmosphere. *Nature* **395**, 575–578.

Hourdin, F., O. Talagrand, R. Sadourney, R. Courtin, D. Gautier, and C. P. McKay 1995. Numerical simulation of the general circulation of the atmosphere of Titan. *Icarus* **117**, 358–374.

Khare, B. N., C. Sagan, E. T. Arakawa, F. Suits, T. A. Callcott, and M. W. Williams 1984. Optical constants of organic tholins produced in a simulated Titanian atmosphere: From soft X-ray to microwave frequencies. *Icarus* **60**, 127–137.

Kouvaris, L. C., and F. M. Flasar 1991. Phase equilibrium of methane and nitrogen at low temperatures: Application to Titan. *Icarus* **91**, 112–124.

Lai, O., J-P. Veran, F. J. Rigaut, D. Rouan, P. Gigan, F. Lacombe, P. J. Lena, R. Arsenault, D. A. Salmon, J. Thomas, D. Crampton, J. M. Fletcher, J. R. Stilburn, C. Boyer, and P. Jagourel 1997. CFHT adaptive optics: First results at the telescope. *SPIE* **2871**, 859–870.

Lemmon, M. T., E. Karkoschka, and M. Tomasko 1993. Titan's rotation: Surface feature observed. *Icarus* **103**, 329–332.

Lemmon, M. T., E. Karkoschka, and M. Tomasko 1995. Titan's rotational light-curve. *Icarus* **113**, 27–38.

Lindal, G. F., G. E. Wood, H. B. Hotz, D. N. Sweetnam, V. R. Eshelman, and G. L. Tyler 1983. The atmosphere of Titan: An analysis of the Voyager 1 radio-occultation measurements. *Icarus* **53**, 348–363.

Lockwood, G. W., B. L. Lutz, D. T. Thompson, and E. S. Bus 1986. The albedo of Titan. *Astrophys. J.* **303**, 511–520.

Lorenz, R. D. 1993. The life, death and afterlife of a raindrop on Titan. *Planet. Space Sci.* **41**, 647–655.

Lorenz, R. D., P. H. Smith, M. T. Lemmon, E. Karkoschka, G. W. Lockwood, and J. Caldwell 1997. Titan's north–south Asymmetry from HST and Voyager imaging: Comparisons with models and groundbased photometry. *Icarus* **127**, 173–189.

Lunine, J. I., D. J. Stevenson, and Y. L. Yung 1983. Ethane ocean on Titan. *Science* **222**, 1229–1230.

Magain, P., F. Courbin, and S. Sohy 1998. Deconvolution with correct sampling. *Astrophys. J.* **494**, 472–477.

Meier, R., B. A. Smith, and T. C. Owen 2000. The surface of Titan from NICMOS observations with the Hubble Space Telescope. *Icarus* **145**, 462–473.

Pearl, J., M. Ngoh, M. Ospina, and R. Khanna 1991. Optical constants of solid methane and ethane from 10,000 to 450 cm^{-1}. *J. Geophys. Res.* **96**, 17,477–17,482.

Quirico, E., and B. Schmitt 1997. Near-infrared spectroscopy of simple hydrocarbons and carbon oxides diluted in solid N_2 and as pure ices: Implications for Triton and Pluto. *Icarus* **127**, 354–378.

Rages, K., J. B. Pollack, and P. H. Smith 1983. Size-estimates of Titan's aerosols based on Voyager high-phase-angle images. *J. Geophys. Res.* **88**, 8721–8728.

Rannou, P., C. P. McKay, and S. Lebounois 2001. The thickness of haze in Titan's lower atmosphere determined from fractal microphysical models. Submitted for publication.

Rannou, P., C. P. McKay, R. Botet, and M. Cabane 1999. Semi-empirical model of absorption and scattering of isotropic fractal aggregates of spheres. *Planet. Space Sci.* **47**, 385–396.

Rigaut, F., G. Rousset, P. Kern, J.-F. Fontanella, J.-P. Gaffard, F. Merkle, and P. Léna 1991. Adaptive optics on a 3.6m telescope: results and performance. *Astron. Astrophys.* **250**, 280–290.

Rigaut, F., D. Salmon, R. Arsenault, J. Thomas, O. Lai, D. Rouan, J-P. Véran, P. Gigan, D. Crampton, J. M. Fletcher, J. Stilburn, C. Boyer, and P. Jagourel 1998. Performance of the Canada–France–Hawaii Telescope adaptive optics Bonnette. *Publ. Astron. Soc. Pac.* **110**, 152–164.

Roddier, F. 1988. Curvature sensing and compensation: A new concept in adaptive optics. *Appl. Optics* **27**, 1223.

Roe, H. G., I. de Pater, S. G. Gibbard, B. Macintosh, C. E. Max, and C. P. McKay 2000. Near- and mid-infrared resolved imaging of Titan's atmosphere. *Bull. Am. Astron. Soc.* **32**, 1023. [DPS Abstract]

Saint-Pé, O., M. Combes, F. Rigaut, M. Tomasko, and M. Fulchignoni 1993. Demonstration of adaptive optics for resolved imagery of Solar System objects: Preliminary results on Pallas and Titan. *Icarus* **105**, 263–270.

Samuelson, R. E., and L. A. Mayo 1997. Steady-state model for methane condensation in Titan's troposphere. *Planet. Space Sci.* **45**, 949–958.

Schmitt, B., E. Quirico, and E. Lellouch 1992. Near infrared spectra of potential solids at the surface of Titan. *ESA-SP* **338**, 383–388. [In *Proceedings of the Symposium on Titan, 9–12 September 1991, Toulouse, France.*]

Schmitt, B., E. Quirico, F. Trotta, and W. M. Grundy 1998. Optical properties of ices from UV to infrared. In *Solar System Ices* (B. Schmitt, C. de Bergh, and M. Festou, Eds.), pp. 199–240. Kluwer Academic, Dordrecht, The Netherlands.

Smith, P. H., M. T. Lemmon, R. D. Lorenz, L. A. Sromovsky, J. J. Caldwell, and M. D. Allison 1996. Titan's surface, revealed by HST imaging. *Icarus* **119**, 336–349.

Thompson, W. R., J. A. Zollweg, and D. H. Gabis 1992. Vapor-liquid equilibrium thermodynamics of $N_2 + CH_4$: Model and Titan applications. *Icarus* **97**, 187–199.

Tomasko, M. G. ESA/NASA Cassini Mission Meeting, London, 1984.

Tomasko, M. G., L. R. Doose, P. H. Smith, R. A. West, L. A. Soderblom, M. Combes, B. Bézard, A. Coustenis, C. de Bergh, E. Lellouch, J. Rosenqvist, O. Saint-Pé, B. Schmitt, H. U. Keller, N. Thomas, and F. Gliem 1997. The Descent Imager/Spectral Radiometer (DISR) aboard Huygens.

Véran, J. P., F. Rigaut, H. Maître, and D. Rouan 1997. Estimation of the adaptive optics long exposure point spread function using control loop data. *J. O. S. A. A.* **14**, 3057–3069.

Yung, Y. L., M. Allen, and J. P. Pinto 1984. Photochemistry of the atmosphere of Titan: Comparison between model and observations. *Astrophys. J. Supp.* **55**, 465–506.